2009

H I absorption spectra toward MAGPIS supernova remnant candidates

Adam Kenneth Johanson
Iowa State University

HI absorption spectra toward MAGPIS supernova remnant candidates

by

Adam Kenneth Johanson

A thesis submitted to the graduate faculty

in partial fulfillment of the requirements for the degree of

MASTER OF SCIENCE

Major: Astrophysics

Program of Study Committee:
Charles Kerton, Major Professor
Steven Kawaler
Craig Ogilvie
Cinzia Cervato

Iowa State University

Ames, Iowa

2009

DEDICATION

I dedicate this thesis to my wife Elizabeth and my children Megan and Jack. They are my joy and purpose in life, and everything I do I dedicate to them. I love you to the Moon.

TABLE OF CONTENTS

LIST OF TABLES

LIST OF FIGURES

ACKNOWLEDGEMENTS

I would like to thank my advisor Charles Kerton for his guidance and all he has taught me. I would also like to thank him for his enthusiasm in his research, a quality that made me want to do research in this area. I also appreciate his patience and understanding during my times of difficulty.

ABSTRACT

The Multi-Array Galactic Plane Imaging Survey (MAGPIS) is an ongoing project to map out the northern Galactic plane in the 21 cm radio continuum. The survey identified 30 probable supernova remnant candidates in the Galactic plane from $18^\circ < l < 32^\circ$. H I absorption spectra were taken toward these sources using data from the VLA Galactic Plane Survey (VGPS). Using both circular and hydrodynamical Galactic rotation models, the corresponding distances were calculated. Of the 30 candidates, distances to nine of them were determined, and another eight sources had their distances constrained with upper and lower bounds. Many of these sources have detectable radio recombination line emission toward them, and the possible nature of these sources is discussed.

CHAPTER 1. INTRODUCTION

The Milky Way Galaxy is a collection of a few hundred billion stars, most of which are found in disk 100,000 light years (ly) across and 1,000 ly in thickness. The Sun is located about 26,000 ly (8 kpc) from the Galactic center. The study of the Galactic disk toward the center of the Galaxy is hindered by dust that obscures the visible light on its way toward Earth. However, this dust in the Galactic plane is transparent to radio and infrared wavelengths. Building detectors sensitive to these regions of the electromagnetic spectrum allows astronomers to peer through the obscuring dust and study the inner Galaxy. Among the stars are also extended structures known as H II regions and supernova remnants (SNRs). These objects give valuable insight into the evolution and structure of the Galaxy.

1.1 Supernova Remnants

At the end of its life, a massive star ($\geq 8\ M_{\odot}$) will undergo a violent explosion known as a supernova. This process will also occur for a white dwarf which has accreted enough mass from a companion to push it over the Chandrasekhar limit ($\geq 1.4\ M_{\odot}$). As these stars explode, the expelled material sweeps up the surrounding interstellar medium, producing a shell-like shock front (see Figure 1.1). This shocked, shell structure left over is called a supernova remnant (SNR). The collision between the ambient medium and the swiftly-moving stellar material can create temperatures high enough to produce X-rays. Free electrons in the SNR spiral around magnetic field lines, emitting a spectrum of synchrotron radiation which peaks in the radio.

Supernovae are important for the evolution of the galaxy. Their shocks can compress interstellar material, initiating star formation. They also distribute heavier elements in the interstellar medium driving the chemical evolution of the galaxy. It is primarily supernovae that

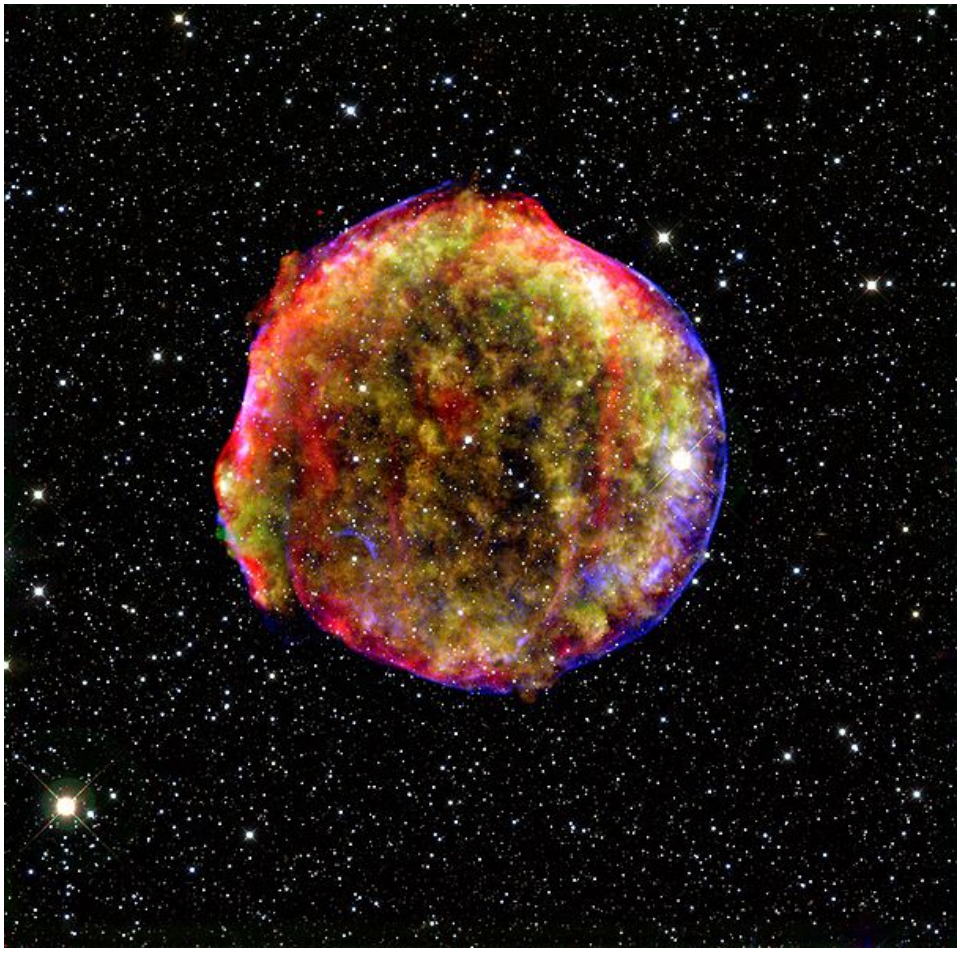

Figure 1.1 Supernova Remnant SN 1572. This supernova was visible to the naked eye and appeared in 1572 AD. This is a composite of *Spitzer* infrared and *Chandra* X-ray images. Credit: NASA/MPIA/Calar Alto Observatory, Oliver Krause

distribute the heavy metals in the interstellar medium needed for terrestrial planet formation. SNRs are also the primary candidates for the production site of cosmic rays (Niemeic et al., 2008).

1.2 H II Regions

As interstellar clouds gravitationally contract, densities and pressures eventually become strong enough to initiate the fusion of hydrogen, and stars are born. The more massive stars ($\geq 8\ M_{\odot}$) emit vast amounts of ultraviolet (UV) radiation. This UV flux ionizes the

surrounding neutral hydrogen gas or H I and creates an ionized plasma. These objects are known as H II regions, being identified with the abundance of ionized hydrogen (see Figure 1.2). As the free electrons pass by the attractive potential of ions, they are deflected, emitting a continuum of radiation visible in the radio. This process is known as thermal bremsstrahlung.

These interstellar clouds are made up of not only hydrogen gas but dust. As the dust absorbs the UV radiation, it heats up and then cools by re-emitting light, much of which is in the infrared part of the spectrum. This thermal emission can be seen in mid- and far-infrared broad-band detectors (18-100 μm). Some of these dust grains are so small that they are basically large molecules of about 20 to 50 atoms. These molecules, known as polycyclic aromatic hydrocarbons (PAHs), are vibrationally excited from the UV photons, and then radiate at infrared bands near 8 μm (Osterbrock, 1989).

Most of the young star forming regions in the Galaxy are located in the spiral arms. The massive, hot stars begin to ionize the surrounding material and form H II regions. H II regions can therefore be used as spiral arm tracers and are useful in mapping out Galactic structure. Since H II regions are visible in the radio and bright in the infrared, this provides a simple first-glance method of separating SNRs and H II regions[1].

1.3 Purpose

In astronomy, all of the physical properties of an object are determined from only a handful of observations, based on a knowledge of the relevant laws of physics. The most basic observation made is the flux of light on a detector within a particular bandwidth. A knowledge of the object's distance combined with the flux can be used to calculate fundamental properties of the object, such as the luminosity. For extended objects, distance allows one to convert an observed angular size to physical dimension. Since finding the distance to astronomical objects is non-trivial, many of their basic properties remain unknown, although all appropriate observations have been made.

A recent survey of the Galactic plane at radio wavelengths by Helfand et al. (2006) produced

[1]For a more in-depth discussion of SNRs and H II regions, see Osterbrock (1989)

Figure 1.2 The Great Orion Nebula. This is the closest H II region to Earth and is visible to the naked eye. This image was taken in multiple wide and narrow optical bands with the *Hubble Space Telescope* and a ground-based 2.2 m telescope. Credit: NASA,ESA, M. Robberto (Space Telescope Science Institute/ESA) and the Hubble Space Telescope Orion Treasury Project Team

a list of probable SNR candidates (see § 2.1). Throughout the Galaxy there is an interstellar medium consisting primarily of H I . At very low densities, H I is capable of emitting radio radiation at a frequency of 1420 MHz (see § 3.1). H I can also absorb the radio emission from background SNRs (or H II regions). By using the equations of radiative transfer (see § 3.2), the observed intensity of the H I along lines of sight toward the SNR candidates can give information about the distances to these objects. Most of the known SNR distances in the Galaxy (Green, 2009) are determined by such H I absorption studies. The primary goal of this thesis is to determine the distance to the objects (or establish distance constraints), and make this information available for use in further studies. Another purpose is to investigate SNR candidates which have detectable radio recombination line emission, typical of H II regions, and give an indication of whether these objects are actually SNRs, by comparing their radio and infrared emission.

CHAPTER 2. GALACTIC PLANE SURVEYS

Astronomers primarily study the heavens from telescopes on Earth, analyzing the visible light reaching the ground through the atmosphere. Optical studies of the Galactic plane are difficult because of the dust that obscures the light coming from most of the Galaxy's constituents. Radio and infrared telescopes are ideal for studying objects toward the center of the Galaxy because dust is transparent at these wavelengths.

One of the disadvantages of radio astronomy is the poor resolution of radio telescopes compared to optical telescopes. For a single aperture, idealized telescope with no atmospheric distortion, the minimum resolvable angular size $\theta_{\rm min}$, is given by the Rayleigh criterion,

$$\theta_{\rm min} = 1.22\frac{\lambda}{D} \tag{2.1}$$

where λ is the observed wavelength, and D is the diameter of the telescope. In order to achieve a resolution of $1''$, an optical telescope observing at $\lambda = 500$ nm needs only to have a diameter of 13 cm. To achieve the same resolution with a radio telescope observing at $\lambda = 21$ cm, the dish must have a diameter of 53 km!

To circumvent this problem radio astronomers use arrays of smaller telescopes to form an interferometer. The resolution of an array is essentially equivalent to a single dish with a diameter equal to the maximum separation of two elements in the array. Greater sensitivity and image quality can be obtained with more telescopes of larger size. The largest radio telescope array is the Very Large Array (VLA) located in the New Mexico desert. The VLA is a system of 27 radio antennas that can be used in different configurations to create high resolution radio images of the sky. The VLA has been used to create surveys of the Galactic plane, providing new means to study the Galaxy.

The development of satellites gave astronomers the opportunity to build space telescopes,

which operate above the Earth, free from atmospheric distortion and allowing for the study of the sky at wavelengths normally absorbed by the atmosphere. The *Spitzer Space Telescope* is one such telescope that has been used to survey the Galactic plane in the infrared. This work uses data from Galactic plane surveys using the VLA and *Spitzer*.

2.1 VGPS and MAGPIS

The VLA Galactic Plane Survey (VGPS; Stil et al., 2006) is a $1'$ resolution survey of 1420 MHz continuum emission and 21 cm H I line emission in the first quadrant from Galactic longitude $18^\circ < l < 67^\circ$ and Galactic latitude $|b| \leq 1.3^\circ$. The H I spectra have a velocity resolution of 1.56 km s^{-1} and a channel spacing of 0.824 km s^{-1}. Short-spacing line and continuum data were provided by the 100 m Green Bank Telescope (GBT) and the Effelsberg 100 m telescope respectively.

The Multi-Array Galactic Plane Imaging Survey (MAGPIS) is an ongoing $6''$ resolution 21 cm radio continuum survey of the northern Galactic plane from $5^\circ < l < 65^\circ$ and $|b| \leq 1^\circ$ using the VLA in the B, C, and D configurations. Helfand et al. (2006) presented a list of 49 high-probability SNR candidates within $5^\circ < l < 32^\circ$. Candidates were identified based on the following criteria applied to the VLA and Midcourse Space Experiment (MSX; Price et al., 2001) data. First, the object has a high 20 cm (radio continuum, VLA) to 21 μm (infrared, MSX Band E) flux ratio. This distinguishes the nonthermal emission from SNRs from the thermal emission from H II regions. Second, since SNR spectra typically rise with decreasing frequency, the object should be detected in the available VLA 90 cm data with similar morphology and peak emission. Finally, objects need to have a shell morphology, which is typical for SNRs. The 30 SNR candidates from the MAGPIS survey in the overlapping VGPS region from $18^\circ < l < 32^\circ$ were analyzed using the available continuum and line data from the VGPS (see Figure 2.1).

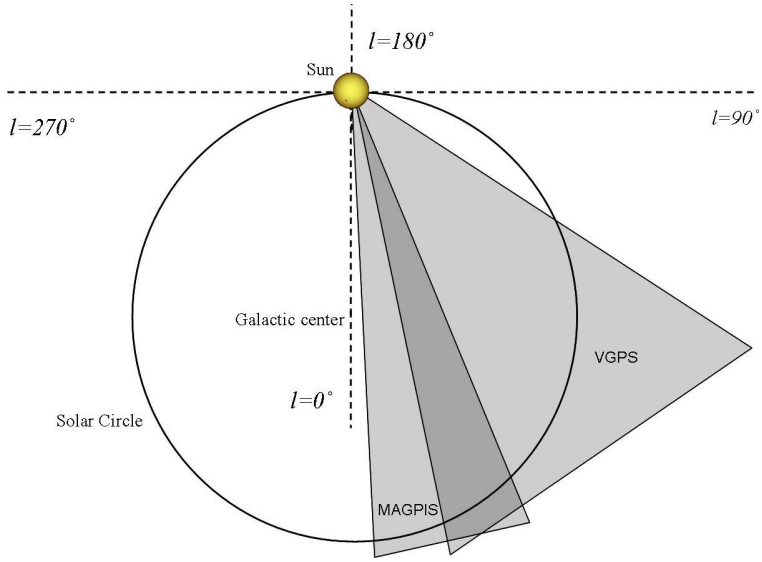

Figure 2.1 Schematic of the Milky Way. The diagram shows the approximate ranges of Galactic longitude l, covered by the MAGPIS and VGPS surveys in the first quadrant. The Galaxy rotates clockwise in this diagram.

2.2 GLIMPSE and MIPSGAL

The *Spitzer Space Telescope* is an infrared telescope launched in an Earth-trailing orbit around the Sun in 2003 (Werner et al., 2004). *Spitzer* completed a $2''$ resolution survey of the Galactic plane from $|l| = 10°$ to $65°$ and $|b| \leq 1°$ called the Galactic Legacy Infrared Mid-Plane Survey Extraordinaire (GLIMPSE; Churchwell et al., 2009). GLIMPSE mapped out this region in four bands in the infrared at 3.6, 4.5, 5.8, and 8.0 μm. The 8 μm band is sensitive to PAH emission and is particularly useful in identifying H II regions.

Carey et al. (2009) used the Multiband Imaging Photometer (MIPS) on *Spitzer* to complete a survey of the Galactic plane called MIPSGAL. This survey covered the same area as the GLIMPSE survey at a wavelength of 24 μm, which is sensitive to the infrared emission from the hot dust in H II regions. Combining this information with the 8 μm GLIMPSE data provides a powerful analytical tool for the identification of H II regions.

CHAPTER 3. H I ABSORPTION SPECTRA

3.1 H I

Most of the interstellar medium consists of neutral hydrogen, or H I . A hydrogen atom may undergo a hyperfine atomic transition wherein the spin of the electron flips to align itself anti-parallel to the proton spin. In doing so the hydrogen atom emits a photon of frequency 1420 MHz, or equivalently, of wavelength 21 cm. The timescale for this transition is on the order of 10^7 years (Binney & Merrifield, 1998, 471), while typical timescales for emission of orbital transition photons in hydrogen are on the order of 10^{-9} s (Griffiths, 2005, 359). Although the atomic transition probability is low, there is so much H I in the Galaxy that the signal is strong enough to be easily detected by radio telescopes on Earth.

As the H I clouds rotate around the Galactic center, some H I is receding away from the Earth, while some is approaching the Earth. The 21 cm radio emission will be Doppler shifted in frequency corresponding to the velocity at which the H I is traveling. The frequency will be shifted higher for radial motion toward the Earth, which is taken to be negative, and frequencies will be shifted to lower values for radial motion away from the Earth, taken to be positive. The shifted position of the 21 cm line thus corresponds to a particular velocity, which gives information about the position of the H I in the Galaxy (see § 3.3). Therefore, instead of discussing measurements in units of line frequencies or wavelengths, units of velocity are used.

The spectrometer used by the VGPS observed the H I line through a 1.1 MHz bandwidth corresponding to velocities from -80 to 150 km s^{-1}. This produced 3-dimensional images known as data cubes, with brightness temperature (T_B, see § 3.2) as a function of Galactic longitude, Galactic latitude, and velocity. Figure 3.1 shows an emission spectrum plotting T_B as a function of velocity. The brightness temperature is a measure of the H I column density

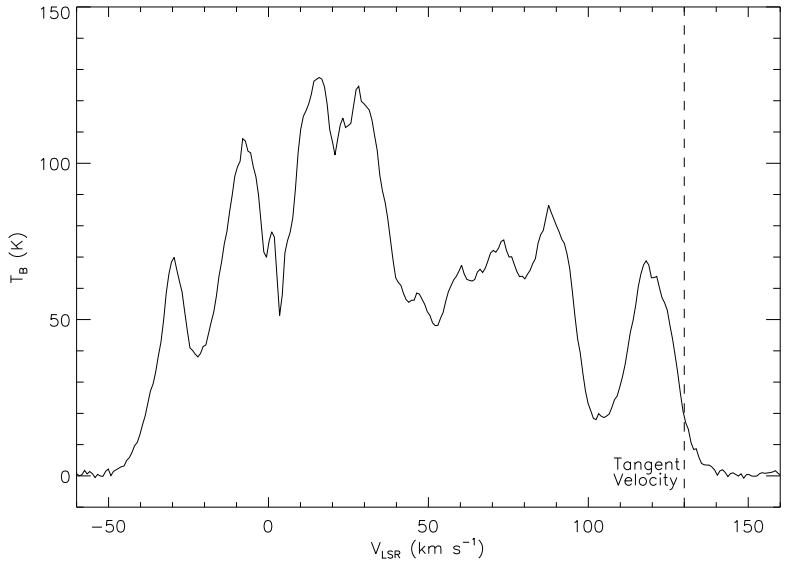

Figure 3.1 H I emission spectrum near G20.4667+0.1500. The spectrum shows the distribution of brightness temperature as a function of velocity. The dashed line shows the position of the tangent velocity.

along the line of sight. For an optically thin gas a simple relationship exists between the column density N(H) and T_B (Binney & Merrifield, 1998, 473):

$$N(\mathrm{H}) = 1.82 \text{ x } 10^{22} \int T_B \, d\nu \text{ atoms m}^{-2}. \tag{3.1}$$

The column density represents the number of atoms in a circular column with a cross sectional area of 1 m^2 between the observer and the source.

3.2 Radiative Transfer

Looking at a spectrum of the H I radiation toward a continuum source reveals regions where the intensity drops below the continuum level. This occurs because the H I between the Earth and the object absorbs some of the incoming radiation. Distance information about the object can be deduced by analyzing the absorption spectra. H I absorption spectra combined with Galactic rotation models are a fundamental means of obtaining distances to SNRs.

H I data cubes map out the intensity of the H I radio emission in units of brightness temperature. Radio astronomers use this unit of intensity primarily because it significantly

simplifies the form of the radiative transfer equation used. In the limit where $h\nu \ll k_B T$, which is almost always valid at radio frequencies, a blackbody will radiate with an intensity spectrum according to the Rayleigh-Jeans law

$$I_\nu(T) = \frac{2\nu^2 k_B T}{c^2}. \tag{3.2}$$

Here, ν is the frequency of the radiation, k_B is Boltzmann's constant, c is the speed of light, and T is the temperature of the blackbody. The brightness temperature is defined as

$$T_B \equiv \frac{c^2 I_\nu(T)}{2\nu^2 k_B}. \tag{3.3}$$

Note that $T_B \neq T$ unless the object really is a blackbody.

The radiative transfer modeling and technique follows from Normandeau (1999). The H I brightness temperature on a line of sight toward a continuum source with a brightness temperature T_c in a continuum subtracted data cube is

$$T_{B,\mathrm{on}}(\nu) = T_s(\nu)(1 - e^{-\tau_\nu}) + T_c e^{-\tau_\nu} - T_c \tag{3.4}$$

where $T_s(\nu)$ is the kinetic temperature of the H I, τ_ν is the optical depth, and ν is the Doppler shifted frequency of the 21 cm line.

The spectrum toward the source is designated the "ON" spectrum. The "OFF" source spectrum is taken along lines of sight just off the source, simulating what the ON spectrum would look like in the absence of a continuum source (i.e. if $T_c = 0$). The OFF spectrum is given by

$$T_{B,\mathrm{off}}(\nu) = T_s(\nu)(1 - e^{-\tau_\nu}). \tag{3.5}$$

We create an opacity spectrum by subtracting the ON and OFF spectra

$$e^{-\tau_\nu} - 1 = \frac{T_{B,\mathrm{on}}(\nu) - T_{B,\mathrm{off}}(\nu)}{T_c} \tag{3.6}$$

Each source has a H I data cube and a corresponding continuum image from the VGPS. The DRAO Export Software Package (Higgs et al., 1997) procedure MEANLEV was used to obtain the ON and OFF spectra. First, MEANLEV accepts a user-defined rectangular region around the source and a limiting brightness temperature contour on the continuum map. It then averages

the points within the contour, weighted proportional to the square of the corresponding T_c, to define the ON spectrum, while the points outside the contour are averaged to define the OFF spectrum. MEANLEV then outputs the ON, OFF, and opacity spectrum for each source.

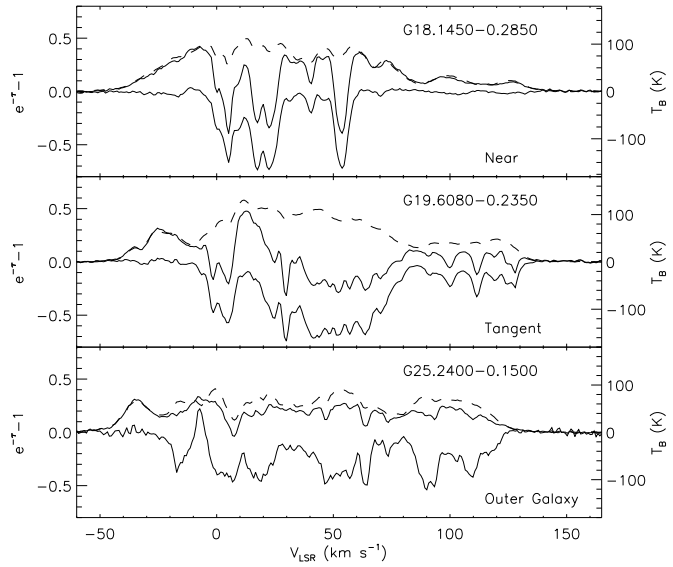

Figure 3.2 Near, Tangent, and Outer Galaxy scenarios. These bright Galactic sources illustrate the three basic types of opacity spectra seen in the first quadrant of the Galaxy. For each source the ON and OFF emission spectra (upper solid line and dashed line respectively, right axis) and the opacity spectrum (lower solid line, left axis) are shown. The upper panel shows an object at the near kinematic distance. The middle panel shows an object at a distance between the tangent point and the far solar circle. The lower panel shows an object beyond the solar circle in the outer Galaxy.

Three types of opacity spectra are possible for sources in the first quadrant of the inner Galaxy. First, absorption could be seen out at negative velocities. This would either place the object in the outer Galaxy, or indicate it was an extragalactic source. The extragalactic case is unlikely because the shell or arc structure of the MAGPIS SNR candidates were resolved at $1'$. Another possibility is to see absorption out to the tangent velocity, where the radial velocity along a particular line of sight reaches a maximum. The third possibility is to see the absorption cease before the tangent velocity. An example of each case is presented in

Figure 3.2. Each of these cases can be translated into distance determinations or constraints based on various Galactic rotation models (see § 3.3).

3.3 Galactic Rotation Models

A model for the motion of gas in the Galaxy can be used to derive a velocity-distance curve that shows the radial velocity of the gas as a function of the distance from the Sun.

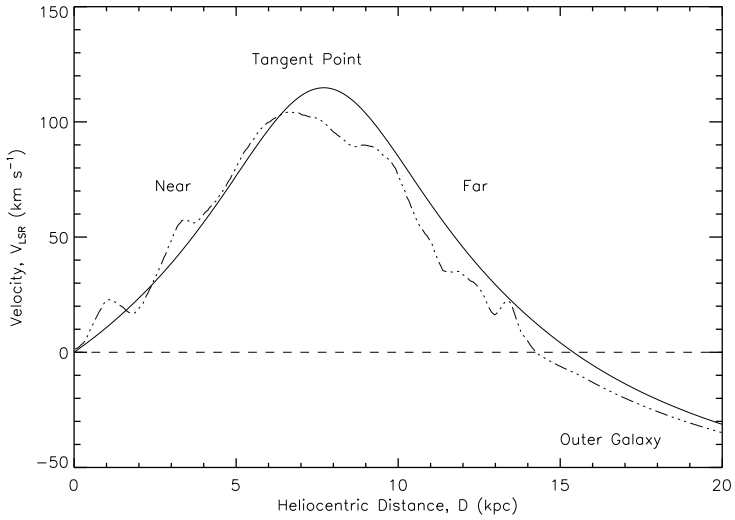

Figure 3.3 Velocity-distance curves for $l = 25°$. The solid line is for a smooth inner Galaxy model plus flat rotation curve and dot-dash line is for the hydrodynamical models of Pohl et al. (2008). The offset in distance between the two models is primarily due to the use of different R_o values. The wiggles in the Pohl et al. (2008) curve are caused by non-circular motions associated with spiral arm and bar structures in the inner Galaxy.

Two different models were used for this study: one based on smooth model fit to tangent point velocities inside the solar radius ($R_o = 8.5$ kpc) with a flat rotation curve ($V_o = 220$ km s^{-1}) beyond the sun, and another based on the hydrodynamical models of Pohl et al. (2008) with $R_o = 7.5$ kpc. To illustrate the typical form of the velocity-distance curves in this part of the Galaxy, Figure 3.3 shows the curves for $l = 25°$. The main offset between the two curves is due to the different values of R_o. The Pohl et al. (2008) model curves typically have a broader peak around the tangent point velocity and the "wiggles" in the curve, associated

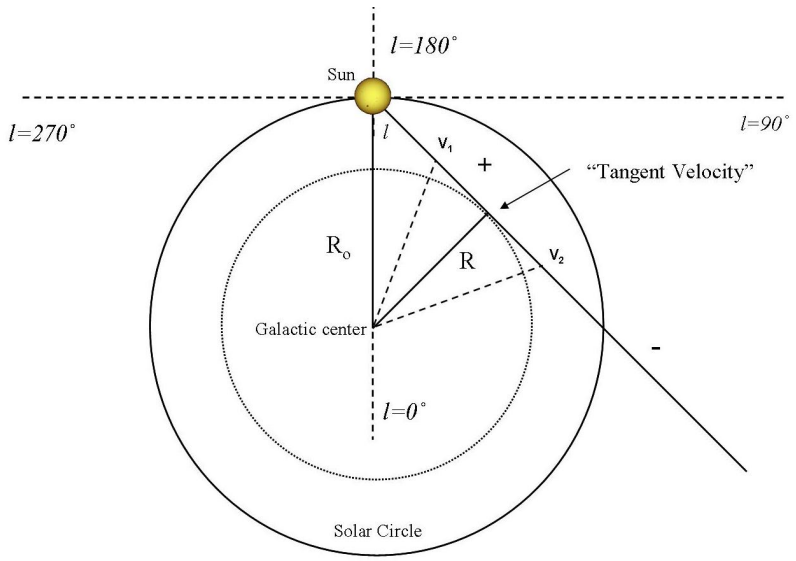

Figure 3.4 Line of sight toward the inner Galaxy. Note that the tangent point occurs where the line of sight is tangent to the circle whose radial vector R intersects the line of sight perpendicularly. This makes it the closest point on the line of sight to the Galactic center, which corresponds to the highest radial velocity in the circular model. The + and - signs indicate areas where the H I has positive and negative radial velocities, respectively. Note that the two velocities v_1 and v_2 are both positive and equal because they are equidistant from the Galactic center.

with non-circular motions in the inner Galaxy, result in multiple "near" and "far" kinematic distances for certain velocities. Both models use flat rotation curves beyond the solar circle so the shapes of the curves for negative velocities are the same.

For each opacity spectrum a distance or distance constraint can be obtained from the models as follows. For objects with absorption out to negative velocities, there is only one corresponding distance beyond the solar circle. For objects with absorption ending closer than the tangent point, the object is at the near kinematic distance. For objects with absorption to the tangent point, it is impossible to assign a unique velocity to that object. The object must be at a minimum distance of that corresponding to the tangent point velocity and at a maximum distance corresponding to where the line of sight intersects the solar circle. This gives an upper and lower bound for the distance. Figure 3.4 shows a schematic of a line of sight through the inner Galaxy.

CHAPTER 4. ANALYSIS

4.1 Characterizing the Opacity Spectrum

Although obtaining an H I opacity spectrum is conceptually simple, in order to obtain useful results care must be taken in identifying the noise level in the spectrum, especially for extended low surface brightness objects where the opacity signal can be low. There are a number of effects that can result in noise in the opacity spectrum which mimic the continuum absorption signal. First, there is instrumental noise in the H I spectra. This can be quantified by calculating the standard deviation of the opacity spectrum in the spectrometer end channels which correspond to velocities where there is no H I . This error estimate is denoted $\sigma_{\rm base}$.

Second, there is a more dominant uncertainty related to the determination of the OFF spectrum. The method by which the opacity spectrum is determined is based on the assumption that the distribution of H I is uniform. It can be seen in Figure 4.1 that this is not always a good approximation. Often there are small-scale variations (compared to the region of interest) in the H I structure. Because MEANLEV averages over the pixels within the region, the variations can cause errors in the determination of the ON and OFF spectra. For example, consider a small, dense, H I cloud in the region of interest. If the cloud is outside of the chosen contour, it introduces an error in the OFF spectrum. The determination of the OFF spectrum is too high, and since the opacity spectrum is a measure of the ON-OFF, it creates a feature which mimics absorption. If the cloud happens to move into the ON spectrum in the next velocity channel, the ON would be too high and it would be possible to obtain what would appear to be emission features in the opacity spectrum. Because the ON spectrum is weighted heavily by the continuum brightness temperature, it is not as large a source of error as the OFF spectrum. Therefore, only the variation in the OFF spectrum is considered. This variation

can be characterized as the standard deviation of the brightness temperature of the pixels used in the OFF spectrum. This error estimate is denoted $\sigma_{\rm off}$.

Finally, large-scale (arcminute or larger) coherent variations in the H I brightness temperature structure (e.g. filaments) can mimic an absorption signal (see Figure 4.1). Unfortunately, lines of sight toward some sources may pass near the edge of large H I structures. This can introduce errors similar to the small-scale structures, where the OFF spectrum can be overestimated and the ON underestimated, or vice versa. To quantify this noise signal due to H I structure a nearby region free of any continuum sources is defined and a similar analysis is performed, producing an OFF - OFF spectrum. This characterizes the uncertainty due to the large coherent variations in the H I throughout the galaxy. The standard deviation from the average of this spectrum (excluding the channels where there is no H I) is denoted $\sigma_{\rm H}$.

For absorption features in the opacity spectrum to be believable, the following criteria was enforced. The signal must be larger than what could be expected from fluctuations in the OFF spectrum. The features must also be more than three times the standard deviation in the random noise, and also more than three times the standard deviation of the noise due to the variations in the H I across the Galaxy. The final error estimate is defined as $\sigma_{\rm tot} = \max[3\sigma_{\rm base}, \sigma_{\rm off}, 3\sigma_{\rm H}]$. Absorption-like features with opacity smaller than $\sigma_{\rm tot}$ were ignored in the velocity determination. All absorption features near the $\sigma_{\rm tot}$ cutoff were examined by eye.

Naturally, the stronger the signal, the less important random variations in the hydrogen intensity become. Strong sources have very high signal to noise and the absorption features are very clear. For weaker sources, variations in H I brightness can be as strong as the absorption features themselves, making it nearly impossible to determine the point at where the absorption features end. There seemed to be a cutoff for sources with peak continuum brightness temperatures around 45 K, where the signal became too weak to distinguish all the absorption features.

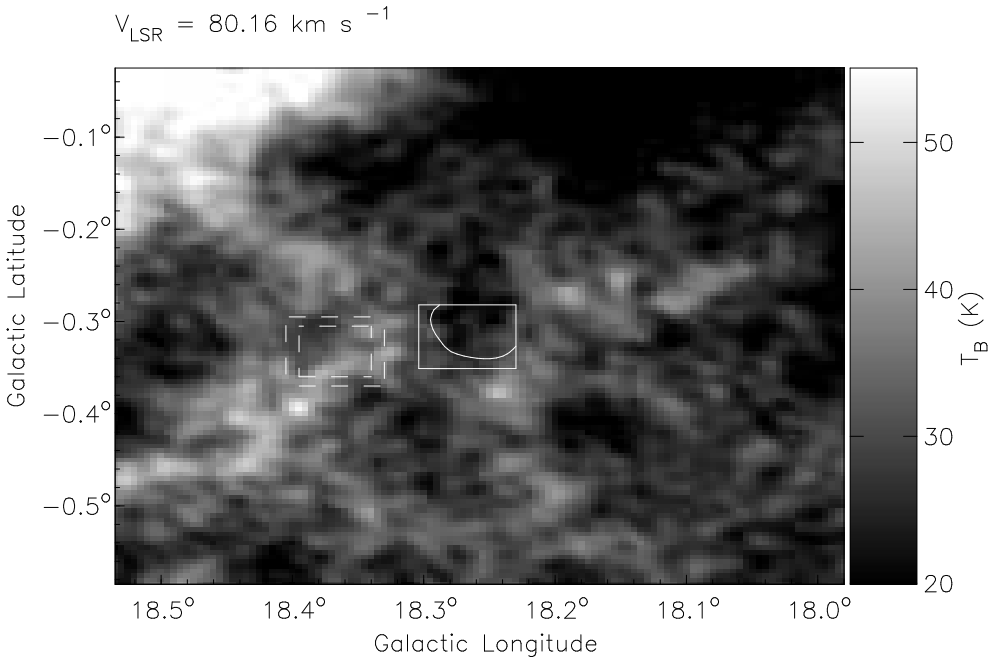

Figure 4.1 False absorption signal. The image shows a velocity channel from a VGPS H I data cube. The central rectangle shows the region of interest for source G18.25-0.31 and the contour indicates the ON and OFF boundary within the region. The large-scale H I structure is such that the ON spectrum is lower than the OFF spectrum producing a false absorption signal. Because there is little small-scale variation in the OFF region, the $\sigma_{\rm off}$ error estimate does not catch this. The $\sigma_{\rm H}$ estimate was developed to quantify the uncertainty caused by these larger-scale variations in H I brightness temperature. The dashed-line boxes to the left show the region used in determining $\sigma_{\rm H}$. The inner box is the false ON region and the outer shows the limits of the OFF.

4.2 Alternative Method

Efforts were made to separate the small-scale structure from the large-scale Galactic emission in hopes to reduce the noise in the opacity spectra due to the H I brightness variations. The H I cubes were smoothed to a Gaussian beam following the procedure of Kothes & Kerton (2002). The smoothed images mapped the large-scale emission from the Galaxy. These large-scale maps were then subtracted from the original H I cube, producing maps of the small-scale structure. Opacity spectra toward the sources could then be taken directly from the small-scale map.

Unfortunately, this method proved unsuccessful in obtaining higher quality opacity spectra. The sources were in general fainter than those studied by Kothes & Kerton (2002). After separating the large-scale from the small-scale features, quantifying the uncertainties in the resulting opacity spectra would have been more difficult. For these reasons the original opacity spectra derived using MEANLEV were used in this study.

CHAPTER 5. RESULTS

Out of the 30 SNR candidates, eight had opacity spectra terminating at velocities before the tangent point, and nine had absorption out to the tangent point. Their spectra are plotted in Figures 5.1 and 5.2.

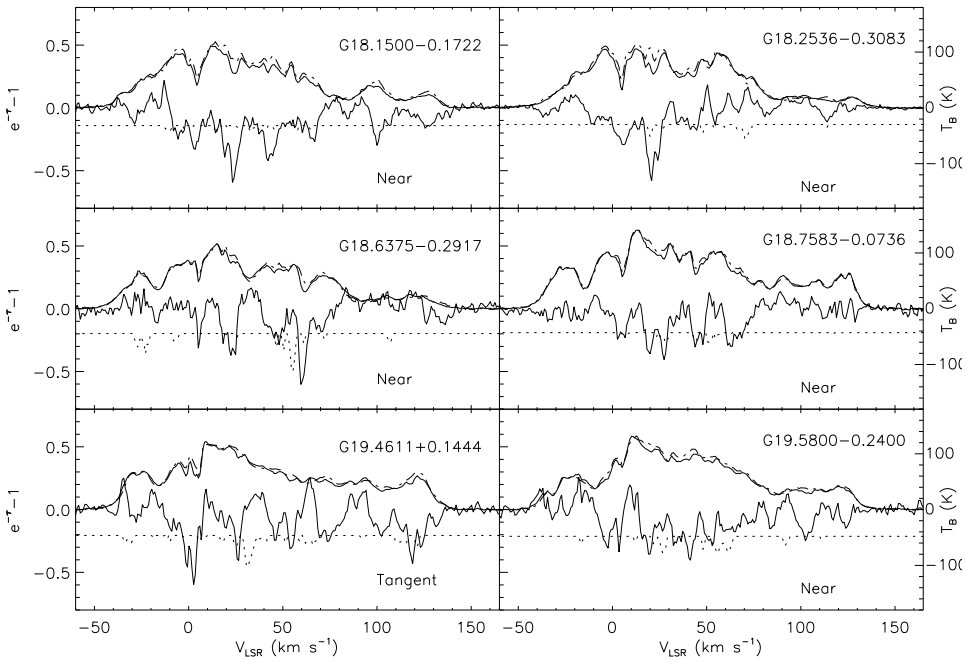

Figure 5.1 H I emission and opacity spectra toward MAGPIS SNR candidates from $18^\circ < l < 19.6^\circ$. For each source the ON and OFF emission spectra (upper solid line and dashed line respectively, right axis) and the opacity spectrum with its error estimate (lower solid line and dotted line respectively, left axis) are shown. The name of the source, as well as whether it is classified as near or tangent is also indicated.

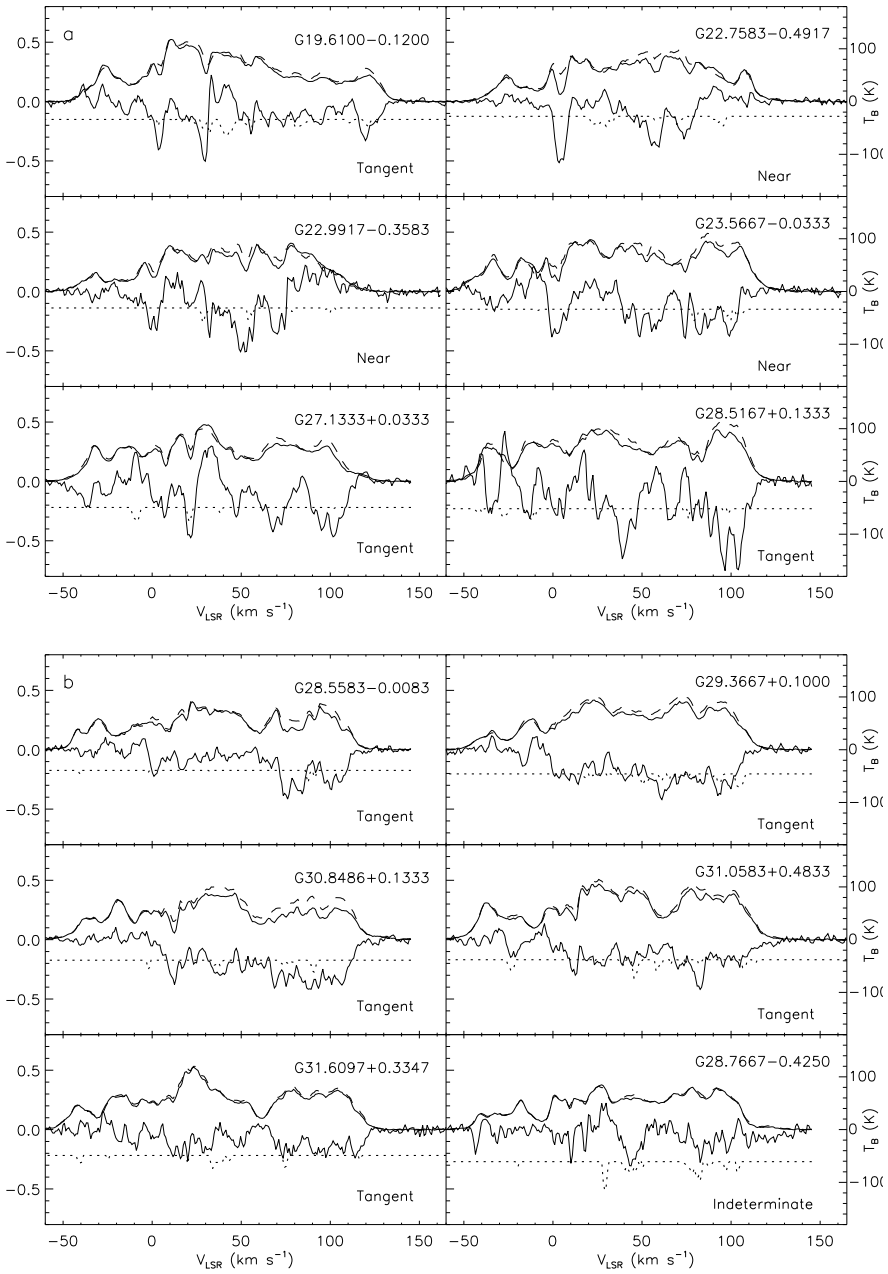

Figure 5.2 H I emission and opacity spectra toward MAGPIS SNR candidates from $19.6° < l < 32°$. The spectra toward G28.7667-0.4250 is shown as an example of a source where the distance was unable to be determined.

The opacity spectra of the remaining candidates had too weak a signal compared to noise levels for a distance determination to be made. Distances for nine of the spectra were determined, eight with opacity spectra corresponding to near kinematic distances, and one tangent point opacity spectrum where a separate determination of the velocity was available allowing us to place the source at the far kinematic distance (see § 5.2). These distances are listed in Table 5.1, and were calculated based on the models described in § 3.3. The error estimates for these distances assume the bulk motions of the H I , apart from their orbital motions, are on the order of 10 km s^{-1} (e.g. Fish et al., 2003). The possibility that objects with absorption within 10 km s^{-1} of the tangent velocity could be at the tangent point was considered. The distances in those cases were constrained with the lower bound corresponding to the near kinematic distance and the upper bound corresponding to the far solar circle. The constraints on the distances to objects with tangent point opacity spectra are listed in Table 5.2. For completeness, Table 5.3 lists the names and peak VGPS continuum brightness temperatures of the sources which were not bright enough to allow us to obtain reliable opacity spectra.

Table 5.1 Distances to SNR Candidates

Name (Gl+b)	$V_{\rm LSR}$ (km s^{-1})	$D_{\rm circ}$ (kpc)	$D_{\rm Pohl}$ (kpc)	$V_{\rm RRL}$[a] (km s^{-1})	Comments
G18.1500-0.1722[b]	102	6.3±0.4	6.2±0.4	-	-
G18.2536-0.3083	45	3.8±0.6	3.5±0.8	50.9	H II [c]
G18.6375-0.2917[b]	62	4.6±0.5	4.8±0.6	71.1	-
G18.7583-0.0736	68	4.9±0.5	4.9±0.6	-	-
G19.5800-0.2400	103	6.3±0.4	6.6±0.6	41.0	H II [d]
G19.6100-0.1200	125	11.6±0.5	11.1±0.3	58.6	H II
G22.7583-0.4917	78	5.1±0.5	4.9±0.4	74.8	H II [e]
G22.9917-0.3583	75	5.0±0.5	4.8±0.4	74.1	H II
G23.5667-0.0333	102	6.3±0.6	6.1±0.7	91.3	d

[a]Velocities obtained from Lockman (1989)
[b]Brogan et al. (2006) SNR
[c]H II indicates the object is actually an H II region
[d]SNR candidate was separated from line of sight H II regions.
[e]SNR candidate could not be separated from line of sight H II regions.

Table 5.2 Constraints on Distances to SNR Candidates

Name (Gl+b)	$D_{\rm circ}$ (kpc)	$D_{\rm Pohl}$ (kpc)	$V_{\rm RRL}{}^a$ (km s^{-1})	Comments
G19.4611+0.1444	6.8-17.5	6.3-16.5	19.8	b
G27.1333+0.0333	6.1-16.2	5.5-15.2	90.2	c
G28.5167+0.1333	6.2-15.9	5.5-14.9	-	-
G28.5583-0.0083	6.5-15.9	5.5-15.0	-	-
G29.3667+0.1000	5.8-15.8	5.2-14.9	-	-
G30.8486+0.1333	6.7-15.6	5.2-14.6	100	b
G31.0583+0.4833	6.6-15.5	5.2-14.6	27.9	d
G31.6097+0.3347	6.6-15.4	5.2-14.6	-	-

[a]Velocities obtained from Lockman (1989)
[b]SNR candidate was separated from line of sight H II regions.
[c]No infrared emission is associated with this source
[d]SNR candidate could not be separated from line of sight H II regions.

5.1 Radio Recombination Lines

Lockman (1989, L89 hereafter) looked at radio recombination lines (RRL) from nearly 500 radio sources in search for H II regions. He obtained velocities for many sources, including some of the SNR candidates identified by the MAGPIS survey. Radio recombination lines are emitted when an electron recombines with a proton. The electron cascades down the available energy levels on its way to the ground state. As it does so, it emits photons with energies corresponding to the differences in the energy levels. The high-order energy levels emit photons with radio frequencies.

Surprisingly 16 of the 30 SNR candidates have detectable radio recombination line (RRL) emission reported in the L89 survey done with the NRAO 43 m (140 ft) telescope ($3'$ beam). Strong RRL emission from SNRs is not expected (Downes & Wilson, 1974; Foster et al., 2006) and the association with the SNR candidates is likely due to either emission from unrelated H II regions close to the SNR or the misclassification of the SNR candidate. The first case is possible given the inner Galaxy location of the candidate and the beam size difference between the RRL survey and MAGPIS. Misclassification is most likely related to the relatively poor

Table 5.3 SNR Candidates With Unknown Distances

Name (Gl+b)	Peak T_B (K)	Comments
G19.5917+0.0250	29	-
G19.6600-0.2200	42	H II [a]
G20.4667+0.1500[b]	35	-
G21.5569-0.1028[b]	24	-
G21.6417+0.0000	29	-
G22.3833+0.1000	34	-
G24.1803+0.2167	37	H II
G25.2222+0.2917	38	-
G28.3750+0.2028	31	-
G28.7667-0.4250	26	-
G29.0667-0.6750	28	H II
G29.0778+0.4542	41	-
G31.8208-0.1222	37	-

[a]H II indicates the object is actually an H II region
[b]Brogan et al. (2006) SNR

sensitivity of the MSX Band E data which may result in missing associated infrared emission. These sources were reinvestigated using higher resolution and sensitivity data from the *Spitzer* GLIMPSE (Benjamin et al., 2003) and MIPSGAL (Carey et al., 2009) surveys[1]. Tables 5.1 and 5.2 indicate the velocity of any associated RRL emission and specify which candidates are actually H II regions.

5.2 Notable Sources

G18.25-0.31 This object has a 3′ diameter shell structure in the MAGPIS 20 cm radio image. L89 reported a RRL detection toward a part of the shell which corresponds to an extremely bright arc of mid-infrared emission visible in the MSX 21 μm image and saturated in the MIPSGAL 24 μm . The GLIMPSE 8 μm images show that the shell of radio emission is surrounded by PAH emission, a structure typically seen for H II regions. G18.25-0.31 is an

[1]False-color RGB images of the various *Spitzer* and MAGPIS data sets can easily be created using the MAGPIS website, http://third.ucllnl.org/gps/index.html

H II region and it is suggested that the bright mid-infrared arc could be an associated massive young stellar object.

G18.64-0.29 This object shows a 4′ long arc in the MAGPIS 20 cm radio image. The MSX 21 μm shows no detectable analog. The GLIMPSE 8 μm shows faint diffuse emission throughout the surrounding region. The MIPSGAL 24 μm band, however, clearly shows a structure analogous to the radio arc. A spectral index study done by Brogan et al. (2006) identified this object as a SNR, but L89 was able to obtain RRL measurements toward this source and he identified it as an H II region. It is possible that the RRL detection is associated with the nearby large W39 H II region.

G19.46+0.14 The MAGPIS radio image shows a diffuse 4′ diameter shell with two brighter compact sources in the line of sight. The brighter of the two compact regions are visible in the MSX 21 μm image. GLIMPSE 8 μm and MIPSGAL 24 μm show a PAH shell and dust emission associated with both compact sources, indicating they are H II regions. The RRL detection reported by L89 is no doubt associated with these H II regions. The two compact sources were masked out of the area when the opacity spectrum was taken. The diffuse shell is surrounded on the lower part by 8 μm emission, but not in the upper portion. Since it lacks a full ring of PAH emission and lacks 24 μm emission, the shell is probably a SNR.

G19.58-0.24 and G19.66-0.22 A very bright H II region sits in the center of these two SNR candidates. The MAGPIS radio image shows two shell structures on opposite edges of the H II region. The MSX 21 μm image shows emission along the edges close to the central H II region, following the boundaries of the SNR candidates. However, there is no other 21 μm emission along the outer edges or in the shells. The MIPSGAL 24 μm image supports the MSX data. The GLIMPSE data show something similar, with PAH emission following the edges of the shells closest to the H II region and fading toward the outer regions. RRL emission was detected by L89 toward this region. An opacity spectrum toward the H II region shows

absorption out to the tangent velocity, indicating it is located at the far kinematic distance. The bright H II region was masked out of the data when the opacity spectra for the two SNR candidates were obtained. The opacity spectrum toward G19.58-0.24 indicates it is located at the near kinematic distance. The signal to noise ratio toward G19.66-0.22 was too low to obtain a reliable opacity spectrum. The H II region is simply a background object not associated with the SNR candidates, which are also believed to be H II regions because of associated infrared emission at both 8 and 24 μm.

G19.61-0.12 The MAGPIS radio data show a relatively compact bright region and a prominent northern arc. These two primary features are not distinguishable at the resolution of the VGPS. The MSX and MIPSGAL data show bright diffuse emission throughout the region, except for the northern arc. The GLIMPSE 8 μm image, however, shows associated emission lining the edges of the entire region, including the northern arc. L89 reported a RRL detection toward this region. This is an H II region with absorption out to the tangent point, placing it at the far kinematic distance corresponding to L89's measurement (see Table 5.1).

G20.47+0.15 This source looks like a 8′ diameter shell in the MAGPIS radio image. The MSX 21 μm data show no associated emission, but the corresponding 24 μm MIPSGAL data show emission with the same structure as the radio data. The 8 μm emission is faint and shows no shell surrounding the region. The source was too faint to obtain a reliable spectrum. L89 was able to detect RRL emission, but Brogan et al. (2006) identified this source as a SNR from a spectral index study. The lack of a PAH shell leads to the conclusion that the source is a SNR.

G22.38+0.10 The radio data from MAGPIS show a faint arc structure near a bright, compact source. The MSX 21 μm infrared data show emission from the compact source, indicating an H II region. The more sensitive MIPSGAL infrared data show a complex system of H II regions with two prominent arcs, one of which is oriented along the radio arc, but is much smaller in size. L89 obtained a RRL detection and may have picked up the smaller arc

in the line of sight of the radio arc. The GLIMPSE data show PAH emission associated with the complex system including the two infrared arcs but not the larger radio arc. The larger radio arc is a SNR, but the complexity of the system prevented a reliable spectrum from being obtained.

G22.76-0.49 The MAGPIS radio image shows a bright compact region and two different arc structures. Strong infrared emission in MSX and MIPSGAL images shows that the compact source is an H II region. The arcs are not visible in the MSX or MIPSGAL data, but the GLIMPSE data show 8 μm emission throughout the entire region, following the arc edges, leading to the conclusion that they are part of another H II region. It is unlikely that the arcs are associated with the compact H II region, because they are invisible in the 24 μm image. Unfortunately, these arc structures could not be separated from the compact H II region at the VGPS resolution. The velocity obtained from the opacity spectrum matched the L89 RRL measurements toward the system.

G22.99-0.36 The MAGPIS radio image of this source shows a $3'$ diameter shell. This shell is not visible in the MSX 21 μm image. The shell is clearly visible in the MIPSGAL data however, and the GLIMPSE data show the PAH emission perfectly outlining the shell. L89 obtained a RRL velocity matching that obtained from the opacity spectrum. This object is an H II region.

G23.57-0.03 The MAGPIS radio image shows a faint, large $8'$ diameter shell, with a brighter compact region in the line of sight. The MSX 21 μm data show that the compact region is a H II region in the line of sight toward the SNR candidate. L89 also measured a RRL velocity toward the object. This area was masked out of the data when the opacity spectrum was obtained. The MIPSGAL and GLIMPSE data show no corresponding emission with the large shell, so it is a SNR.

G24.18+0.22 The MAGPIS radio image shows a $5'$ diameter shell with slightly brighter emission from a more compact region near the bottom. The MSX 21 μm data show no

associated infrared emission with this region. The MIPSGAL data show that the compact source has associated 24 μm emission, but not the shell as a whole. L89 obtained a RRL measurement toward the lower compact region. The GLIMPSE image shows 8 μm emission surrounding the larger shell. The signal to noise ratio was too low to obtain a reliable opacity spectrum. Both the compact region and larger shell are probably H II regions.

G27.13+0.03 The MAGPIS radio image shows a prominent arc 10′ in length. There is no corresponding infrared emission at any wavelength from any of the other surveys, which makes the L89 RRL detection very curious. The absorption in the opacity spectrum went out to the tangent point, so there is not another measurement of the source's velocity to compare with the RRL data. There is a relatively faint compact H II region 3′ away from L89's telescope pointing, which may account for the RRL detection. There is no doubt though that G27.13+0.03 is a SNR.

G29.07-0.68 The 20 cm MAGPIS radio image shows a 10′ diameter shell. The MSX 21 μm data show no associated infrared emission with this region. The MIPSGAL data show that the center is filled with 24 μm emission and the GLIMPSE data show that the entire region is surrounded by PAH emission. L89 obtained a RRL velocity toward this source, which is clearly an H II region. The signal to noise ratio was too low to obtain a useful opacity spectrum toward this source.

G30.85+0.13 There is a 2′ diameter shell in the MAGPIS radio image only 30″ away from a bright, compact source. The bright compact source has associated MSX 21 μm emission, and the MAGPIS and GLIMPSE data also show emission from the compact source identifying it as an H II region. L89 reported a RRL detection toward this region, but it most definitely came from the compact H II region. The H II region was masked out of the data when the opacity spectrum was obtained. There is no associated infrared emission with the shell and it is correctly identified as a SNR.

G31.06+0.48 The MAGPIS radio image of this region shows a complex structure of arcs and compact sources. One prominent arc is distinct from the rest of the complex. The MSX 21 μm data show faint emission from the central region, and the prominent arc is not visible. The MIPSGAL data show several bright, compact H II regions in the complex, much more than is visible in the MSX data. There is no corresponding emission from the arc structure in the MIPSGAL or the GLIMPSE data. The GLIMPSE data do show emission throughout the complex region. The arc and the central region could not be separated in the VGPS data. L89 measured RRL emission from the central complex, and absorption to the tangent point places the complex at the far kinematic distance. The prominent arc is probably a SNR.

CHAPTER 6. SUMMARY AND CONCLUSIONS

Using data from the VGPS, H I absorption and emission spectra were taken toward MAGPIS SNR candidates. The radial velocities and corresponding distances to nine of these sources were determined from the resulting opacity spectra. For eight sources only lower and upper limits on their distance could be determined. All of the SNR candidates with RRL detections reported in L89 were reexamined and it was determined that eight of the sources were not SNRs, but rather H II regions. Since L89 had a separate velocity determination for these objects, the far and near kinematic distance ambiguity could be resolved with the opacity spectra. The primary reason for misidentification was the low sensitivity of the MSX Band E data originally used for infrared detection. The more sensitive MIPSGAL 24 μm data and the GLIMPSE 8 μm data, tracing the PAH emission, proved to be very useful in identifying H II regions.

It is clear that the more sensitive GLIMPSE 8 μm and MIPSGAL 24 μm data will produce a better indication of thermal sources as MAGPIS continues its survey covering the rest of the northern Galactic plane and identifies additional SNR candidates. H I absorption spectra from the VGPS can be used to determine the distances to many of the candidates, but higher resolution H I data, matching the resolution of the MAGPIS continuum data, would be very useful for determining distances to new SNR found in complex regions where it is difficult to separate H II region and SNR emission.

BIBLIOGRAPHY

Benjamin, R. A., et al. 2003, PASP, 115, 953

Binney, James & Merrifield, Michael 1998, Galactic Astronomy, (Princeton, New Jersey: Princeton University Press)

Brogan, C. L., Gelfand, J. D., Gaensler, B. M., Kassim, N. E., & Lazio, T. J. W. 2006, ApJ, 639, L25

Carey, S. J., et al. 2009, PASP, 121, 76

Churchwell, E., et al. 2009, PASP, 121, 213

Downes, D., & Wilson, T. L. 1974, A&A, 34, 133

Fish, V. L., Reid, M. J., & Wilner, D. J., Churchwell, E. 2003, ApJ, 587, 701

Foster, T., Kothes, R., Sun, X. H., Reich, W., & Han, J. L. 2006, A&A, 454, 517

Green, D. A. 2009, Bulletin of the Astronomical Society of India, 37, in press.

Griffiths, David J. 2005, Introduction to Quantum Mechanics (2nd ed.; Upper Saddle River, New Jersey: Pearson Prentice Hall)

Helfand, D. J., Becker, R. H., White, R. L., Fallon, A., & Tuttle, S. 2006, AJ, 131, 2525

Higgs, L. A., Hoffmann, A. P., & Willis, A. G. 1997, in ASP Conf. Ser. 125, Astronomical Data Analysis Software and Systems VI, ed. G. Hunt & H. E. Payne (San Francisco, CA: ASP), 58

Kothes, R., & Kerton, C. R. 2002, A&A, 390, 337

Kuchar, T.A., & Bania, T.M. 1990, ApJ, 352, 192

Lockman, F.J. 1989, ApJS, 71, 469

Niemeic, J., Pohl, M., Stroman, T., Nishikawa, K. 2008, ApJ, 684, 1174

Normandeau, M. 1999, AJ, 117, 2440

Osterbrock, Donald E. 1989, Astrophysics of Gaseous Nebulae and Active Galactic Nuclei, (Sausalito, CA: University Science Books)

Pohl, M., Englmaier, P., & Bissantz, N. 2008, ApJ, 677, 283

Price, S. D., Egan, M. P., Carey, S. J., Mizuno, D. R., & Kuchar, T. A. 2001, AJ, 121, 2819

Stil, J.M., et al. 2006, AJ, 132, 1158

Werner, M. W., et al. 2004, ApJS, 154, 1